Fractal Antennae and Coherence

Juan A. Valdivia
Code 692,
Nasa Goddard Space Flight Center
Greenbelt, MD 20771
alejo@roselott.gsfc.nasa.gov
(301) 286-3545

December 16, 1997

Abstract

Fractal antennae have very special properties:

(1) They are broad band antennae, i.e. they radiate, and detect, very efficiently for a wide range of frequencies. The frequency range is specified by the smallest and largest size present in the antenna. The radiation, and hence the detection, efficiency depends slowly on frequency between these two limits.

(2) They can display considerable gain over normal dipole type of antennae and this gain depends slowly on frequency over a large frequency range. This antenna gain can be related to the spatio-temporal structure of the radiation pattern.

(3) They can display spatial structure. The spatial structure is also related to the antenna gain, as the antenna concentrate radiated power in certain postions and now in others. This spatial structure can be very useful when directionality is required.

1 Fractal Antennae and Coherence

For the purposes of this work, we assume that a fractal antenna can be formed as an array of "small" line elements having a fractal distribution in space. Such description is consistent with our understanding of fractal discharges and lightning observations as discussed by *LeVine and Meneghini* [1978], *Niemeyer et al.* [1984], *Sander* [1986], *Williams* [1988], and *Lyons* [1994]. Appendix A develops the theory for the calculation of the fields produced by a fractal antenna composed of small line elements and for the calculation of the array factor in the far field of the fractal.

Fractals are characterized by their dimension. It is the key structural parameter describing the fractal and is defined by partitioning the volume where the fractal lies into boxes of side ε. We hope that over a few decades in ε, the number of boxes that contain at least one of the discharge elements will scale as $N(\varepsilon) \sim \varepsilon^{-D}$. It is easy to verify that a point will have $D = 0$, a line will have $D = 1$ and a compact surface will have $D = 2$. The box counting dimension [*Ott*, 1993] is then defined by

$$D \simeq \frac{\ln N(\varepsilon)}{\ln(\frac{1}{\varepsilon})} \tag{1}$$

For a real discharge there is only a finite range over which the above scaling law will apply. If ε is too small, then the elements of the discharge will look like one-dimensional line elements. Similarly, if ε is too large, then the discharge will appear as a single point. It is, therefore, important to compute D only in the scaling range, which is hopefully over a few decades in ε. The fractal dimension will be an important parametrization for the fractal discharge models that we will explore later, and will impact significantly the intensity and spatial structure of the radiated pattern.

We consider a fractal antenna as a non uniform distribution of radiating elements (Fig. 1). Each of the elements contributes to the total radiated power density at a given point with a vectorial amplitude and phase, i.e.

$$\mathbf{E} \cdot \mathbf{E}^* \sim (\sum_{n=1}^{N} \mathbf{A}_n e^{i\phi_n}) \cdot (\sum_{m=1}^{N} \mathbf{A}_n e^{i\phi_m})^* = \sum_{n,m} (\mathbf{A}_n \cdot \mathbf{A}_m^*) e^{i(\phi_n - \phi_m)} \tag{2}$$

The vector amplitudes $\mathbf{A}_n$ represent the strength and orientation of each of the individual elements, while the phases ϕ_n are in general related to the spatial distribution of the individual elements over the fractal, e.g. for an oscillating current of the form $e^{i\omega t}$ the phases vary as $\phi \sim kr$ where $k = \frac{\omega}{c}$ and r is the position of the element in the fractal.

In the sense of statistical optics, we can consider the ensemble average of Eq. (2), using an ergodic principle, over the spatial distribution $P(\phi_1, \phi_2, \phi_3, ..., \mathbf{A}_1, \mathbf{A}_2, \mathbf{A}_3, ...)$ of the fractal elements [*Goodman*, 1985]. For simplicity we assume that the distributions for each of the elements are independent, and also the same, hence

$$G = \sum_{n,m}^{N} \left\langle (\mathbf{A}_n \cdot \mathbf{A}_m^*) e^{i(\phi_n - \phi_m)} \right\rangle = N^2 \left(\frac{\left\langle |\mathbf{A}|^2 \right\rangle}{N} + \frac{N-1}{N} \left| \langle \mathbf{A} \rangle \right|^2 \left| \left\langle e^{i\phi} \right\rangle \right|^2 \right)$$

By requiring that $\left\langle |\mathbf{A}|^2 \right\rangle = \left| \langle \mathbf{A} \rangle \right|^2 = 1$ we obtain that the ensemble average is

$$\langle \mathbf{E} \cdot \mathbf{E}^* \rangle \sim G = N^2 \left(\frac{1}{N} + \frac{N-1}{N} \left| \left\langle e^{i\phi} \right\rangle \right|^2 \right)$$

If the distribution of the phases is uniform (e.g. random) then $< e^{i\phi} >= 0$ and $G = 1/N$. On the other hand, if there is perfect coherence we have $< e^{i\phi} >= 1$

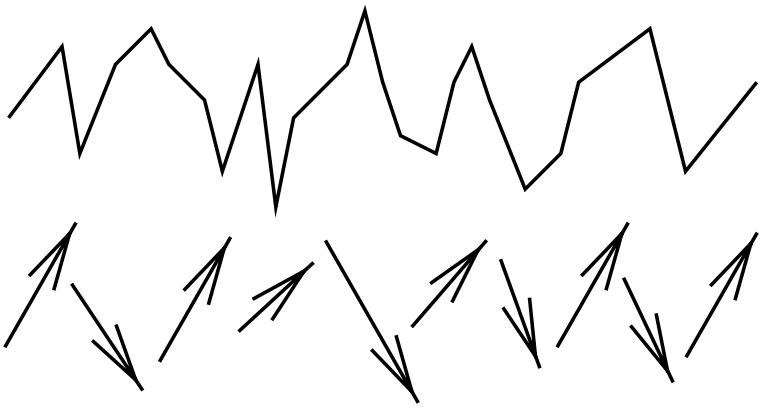

Figure 1: A spatially nonuniform distribution of radiators, each contributiong to the total radiation field with a given phase.

and $G = 1$. In general, a fractal antenna will display a power law distribution in the phases $P_\alpha(\phi) \sim \phi^{-\alpha}$ (multiplied by the factor $1 - e^{-\phi^{-\alpha}}$ so it is finite at the origin), where $\alpha = 0$ corresponds to the uniform distribution case and $\alpha \to \infty$ corresponds to perfect coherence. Figure 2 shows the plot of $\left|\left\langle e^{i\phi} \right\rangle\right|$ as a function of α. It can be seen that a power law distribution of phases, or similarly a power law in the spatial structure, gives rise to partial coherence.

If the distribution of the vector amplitudes does not satisfy the above relations, e.g. the radiators are oriented in arbitrary directions, then the power density will be less coherent due to $\left\langle |\mathbf{A}|^2 \right\rangle \geq |\langle \mathbf{A} \rangle|^2$. A similar result can be achieved by having a power law distribution in the amplitudes. In conclusion, the radiation field from a power law distribution of phases will have a point where the phases from the radiators will add up almost (partially) coherently showing a significant gain over a random distribution of phases. Hence the concept of a fractal antenna.

The partial coherence of the radiators depends on the spatial power law distribution. Such a power law distribution of phases can be visualized with the help of Cantor sets [*Ott*, 1993]. A family of Cantor sets is constructed by successively removing the middle $\eta < 1$ fraction from an interval, taken as [0,1], and repeating the procedure to the remaining intervals (see Fig. 3). At the n^{th} step, a radiator is placed at the mid-point of each of the remaining intervals.

Note that for $\eta = 0$ we obtain a uniform distribution of elements, but for $\eta \neq 0$ the radiators are non-uniformly distributed, and in fact the spatial distribution follows a power law that can be described by its fractal dimension. Suppose that for ε we require $N(\varepsilon)$ intervals to cover the fractal, then it is clear that with $\varepsilon' \to \frac{\varepsilon}{2}(1 - \eta)$ we would require $2N(\varepsilon')$ intervals to cover the fractal. But the

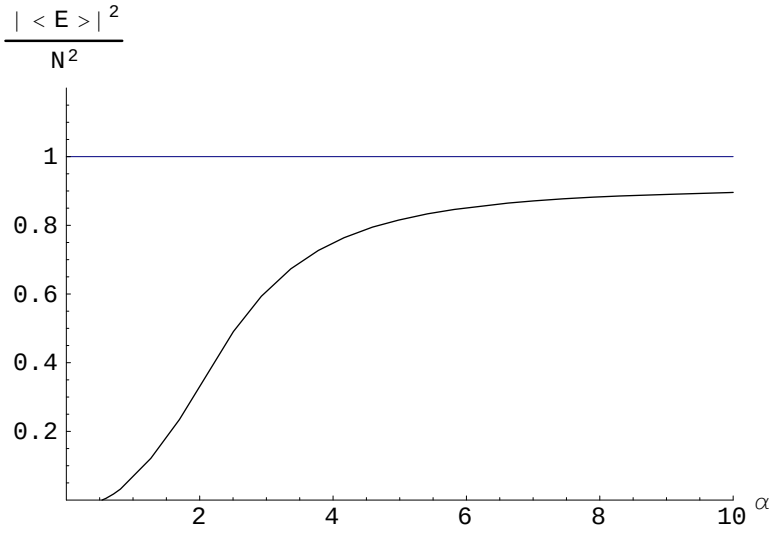

Figure 2: A plot of $\left|\left\langle e^{i\phi}\right\rangle\right|^2$ as a function of α.

fractal is the same, therefore, $N(\varepsilon) = 2N(\varepsilon^{'})$. From the scaling $N(\varepsilon) \sim \varepsilon^{-D}$ we obtain that the dimension is given by

$$D = -\frac{\ln 2}{\ln(\frac{1-\eta}{2})}$$

We can go further, and write a formula for the radiation field due to the $\eta-$Cantor set of radiators. Note that if at the n^{th} step we have the radiators placed at the sequence of points $S_n = \{x_i | i = 1, ..., 2^{n-1}\}$ then at the $\mathrm{n}^{th}+1$ step each radiator at x_i will be replaced by two radiators at $x_i \pm \frac{1}{2^{n+1}}(1-\eta)^{n-1}(1+\eta)$ generating the sequence $S_{n+1} = \{x_i | i = 1, ..., 2^n\}$. Since we start with $S_1 = \{\frac{1}{2}\}$ the sequences S_n at the n^{th} step are trivially constructed. The radiation field (see Eq. (1)) from this $\eta-$Cantor set at the n^{th} step can then be written as

$$E = \sum_{m=1}^{n} (-1)^m \mu_m e^{ikLa\ x_m + i\phi_m} \tag{3}$$

where $k = \frac{\omega}{c}$, L is the spatial extent of the fractal, $a = \widehat{\mathbf{x}} \cdot \widehat{\mathbf{r}}$ is the angular position of the detector, and ϕ_m (taken as zero) is the phase of the m^{th} element. The radiators are given a strength proportional to the measure μ_i (or length) of the segment which defines it.

The space dependence of the radiation fields is plotted in Fig. (4)a-b for $\eta = 1/3$ ($D = 0.63$) and $\eta = 0$ ($D = 1$) respectively, where the sets have been taken to the 5^{th} level. The most relevant issue for our purposes is the fact that there is a direction at which phases add coherently (partially) for $\eta = 1/3$ while this does not happen for the homogeneous case $\eta = 0$.

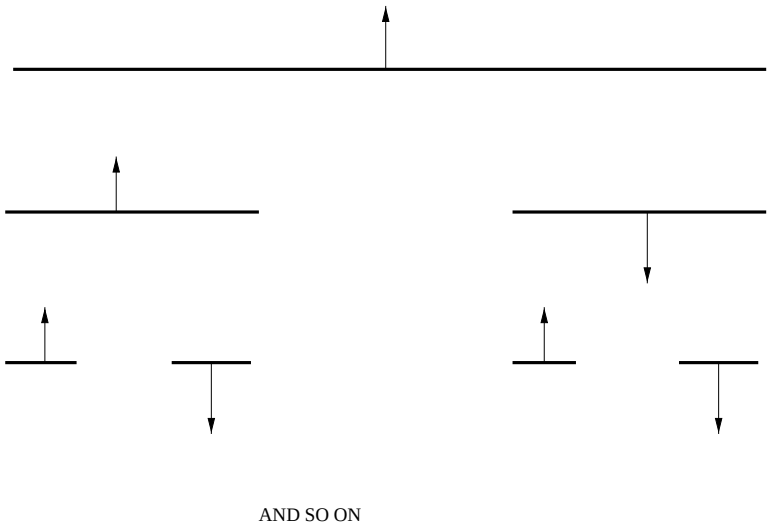

Figure 3: The construction of the fractal distribution of the radiators from the $\eta-$Cantor set.

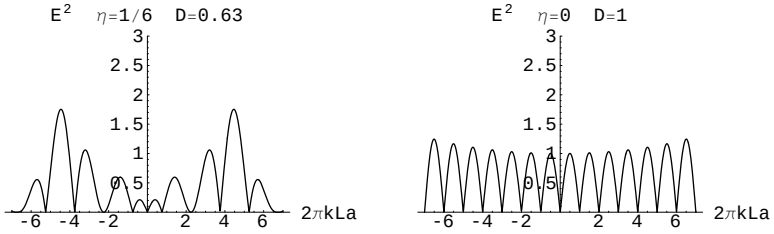

Figure 4: The spatial dependence of the radiation fields for (a) $\eta = 1/3$, $D = 0.63$ and (b) $\eta = 0$, $D = 1$.

Therefore, partial coherence occurs naturally in systems that have power-law spatial distributions. We are now ready to turn to the properties of fractal antennae with propagating currents. Specifically, how tortuosity and branching can increase the radiated field intensity in some locations as compared with single dipole antennae.

2 Radiation and Simple Fractal Models

To illustrate the properties of fractal antennae compared to those of simple dipole radiators, we take the fractal antenna as composed of small line elements and compute its far field radiation pattern. For an oscillating current $I(t) = I_o e^{-i\omega t}$ that propagates with speed $\beta =$v/c along the antenna, the contribution

from each line element to the total radiation field is (from Eq. (1))

$$\frac{cr\mathbf{E}_n(\mathbf{r},t)}{I_o} = e^{-i\omega t}e^{ikr}\frac{\beta\widehat{\mathbf{L}}_n}{(1-\beta a_n)}e^{ikp_n b_n}e^{i\frac{ks_n}{\beta}}(e^{ikL_n a_n}e^{i\frac{kL_n}{\beta}}-1) \qquad (4)$$

where $a_n = \widehat{\mathbf{L}}_n\cdot\widehat{\mathbf{r}}$, $\mathbf{p}_n$ is the position of the beginning of the line element from the origin, and $b_n = \widehat{\mathbf{p}}_n\cdot\widehat{\mathbf{r}}$. Radiation occurs when there is a change in the direction of the propagating current. Also note that mathematically we can describe a radiator with a nonpropagating current in the non-physical limit $\beta\to\infty$.

In general, the radiation pattern of an antenna can be effectively excited, only by certain frequencies corresponding to the characteristic length scales of the antenna, e.g. $kL\sim 1$ (see Eq. (4)). Therefore, if there is no characteristic size, as in the case of a power law structure, then the antenna will generate an effective radiation pattern for a whole range of frequencies controlled by the smaller and largest spatial scale. Such antenna is called a broad band antenna, and that is why fractal antennae are so important in many applications.

By spatially superposing these line radiators we can study the properties of simple fractal antennae. Of special interest, to our high altitude lightning work, is to compare the radiation pattern of these fractal models with a simple (meaning one line element) dipole antenna.

2.1 Gain Due to Tortuosity

The first element in understanding fractal antennae is the concept of tortuosity in which the path length between two points is increased by requiring that the small line elements are no longer colinear. A simple tortuous model is displayed in Fig. 5, where the parameter ε represents the variation from the simple dipole model (line radiator), i.e. the dipole is recovered as $\varepsilon\to 0$.

Except for the propagation effect, we can observe that this antenna (Fig. 5) can be considered as the contribution from a long line element (a dipole) plus the contribution from a Cantor set of radiators as described in the previous section (see Eq. (3)). Therefore, the tortuosity naturally increases the radiation field intensity, at least in some direction, as compared with the single dipole element.

The field can be written for the structure of 5, with the help of Eq. (4), as the superposition of the 2N line elements, and is given by the normalized field

$$\mathbf{E}(\varepsilon) = \frac{\beta(e^{ikla_x}e^{i\frac{kl}{\beta}}-1)}{(1-\beta a_x)}\widehat{\mathbf{x}} + \frac{\beta e^{ikla_x}e^{i\frac{kl}{\beta}}(e^{ik\varepsilon a_y}e^{i\frac{\varepsilon kl}{\beta}}-1)}{(1-\beta a_y)}\widehat{\mathbf{y}} + \ldots \qquad (5)$$

where $l = \frac{L}{N}$ is the length of the small segments composing the tortuous path, and $a_x = \widehat{\mathbf{x}}\cdot\widehat{\mathbf{r}}$ and $a_y = \widehat{\mathbf{y}}\cdot\widehat{\mathbf{r}}$. It is clear that in the limit $\varepsilon\to 0$ we recover the single dipole radiation pattern. The effect of the tortuosity can now be posed as the behavior of the normalized $\mathrm{P}(\varepsilon) = \mathbf{E}(\varepsilon)\cdot\mathbf{E}^*(\varepsilon)$ for $\varepsilon\neq 0$. In general the analysis can be simplified in the limit for small ε, i.e. $\mathrm{P}(\varepsilon)\simeq \mathrm{P}(0)+\mathrm{P}'(0)\varepsilon+\ldots$. Of course $\mathrm{P}(0)$ is the dipole contribution, and $\mathrm{P}'(0)\varepsilon$ is the change in the radiated power density due to tortuosity. The dipole has a maximum in the radiated

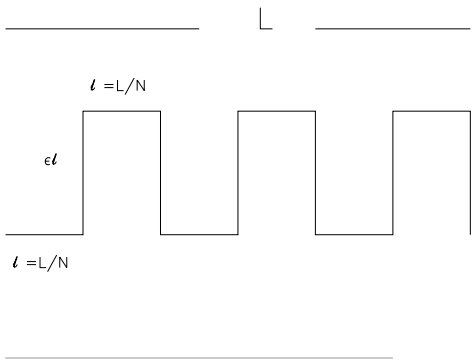

Figure 5: A simple tortuous variation of a line radiator. Note that the antenna will radiate every time there is a change in direction.

power density $\mathrm{P}(0) \simeq \frac{4\beta^2}{(1-\beta a_x)^2}$, while the tortuous contribution goes as $\mathrm{P}'(0)\varepsilon \simeq \frac{4\beta k L \varepsilon}{(1-\beta a_x)^2}\mathrm{f}(a_x, a_y, kL, \beta, N)$. The function f depends on the given parameters, but its maximum is of the order $\mathrm{f} \sim 1$ with clear regions in (a_x, a_y) where it is positive.

For our purposes, the most important contribution comes from the fact that $\mathrm{P}'(0)\varepsilon$ is essentially independent of N and it scales as $\Delta\mathrm{P} \sim \beta k \Delta s = \beta k L \varepsilon$, which corresponds to the increase in the path length of the antenna due to the tortuosity. Such technique can be applied to other geometries, giving essentially the same scaling $\Delta\mathrm{P} \sim \beta k \Delta s$ result. This fact will be extremely relevant in our analysis since lightning has naturally a tortuous path.

2.2 Fractal Tortuous Walk

More generally, a fractal tortuous path can also be constructed in terms of a random walk between two endpoints [*Vecchi, et al.*, 1994]. We start with a straight line of length L, to which the midpoint is displaced using a Gaussian random generator with zero average and deviation σ (usually $\sigma = 0.5 L_i$). The procedure is then repeated to each of the straight segments N times. There is a clear repetition in successive halving of the structure as we go to smaller scales, making this antenna broad band. Figure 6a shows a typical tortuous fractal where the division has been taken to the N=8 level and in which the pathlength s has increased 5 times, i.e. $s = 5L$. We can estimate the fractal dimension by realizing that the total length should go as $L_{tot} \sim L(\frac{s}{\langle \ell \rangle})^{D-1}$, where $\langle \ell \rangle$ is the

average segment size. This formulation is completely equivalent to Eq. (1).

We let an oscillating current, e.g. $I_o e^{i\omega t}$, propagate along the fractal, but in real applications we can imagine the oscillating current lasting for only a finite time $1/\alpha$. In order to have a finite current pulse propagating through the fractal random walk, we let $I(t) = I_o(e^{-\alpha t} - e^{-\gamma t})(1+\cos(\omega t))\theta(t)$ with $\omega = 2\pi\alpha n_f$ and $\theta(t)$ as the step function. Here n_f represent the number of oscillations during the decay time scale $1/\alpha$. We chose the decay parameters as $\alpha = 10^3$ s^{-1} and $\gamma = 2 \times 10^5$ s^{-1}, hence $\gamma/\alpha = 200$, which correspond to realistic parameters for lightning [*Uman*, 1987]. The radiated power density is then computed using Eq. (12) and is shown in Fig. 6b for $n_f = 5$ and $\beta = 0.1$ at the position $a_x = 0$, $a_y = 0$, $r = 60$ km. The dipole equivalent is given by the dashed lines in all 3 panels. The peak in the radiated power density is about 10 times larger than for the dipole case, which agrees well with the results $\frac{P'(0)\varepsilon}{P(0)} \sim \frac{2\pi\alpha\Delta s}{c\beta} n_f \sim 10$ even though the effect from the tortuosity is not small. The larger path length of the tortuous discharge produces an increase in the radiation as compared with a dipole radiator. Of course there is a limit due to energy conservation, but in practical applications we are well under it. The increase in the high frequency components of the radiated field power spectrum (Fig. 6c), as compared with the dipole antenna, will be responsible for the spatially structured radiation pattern.

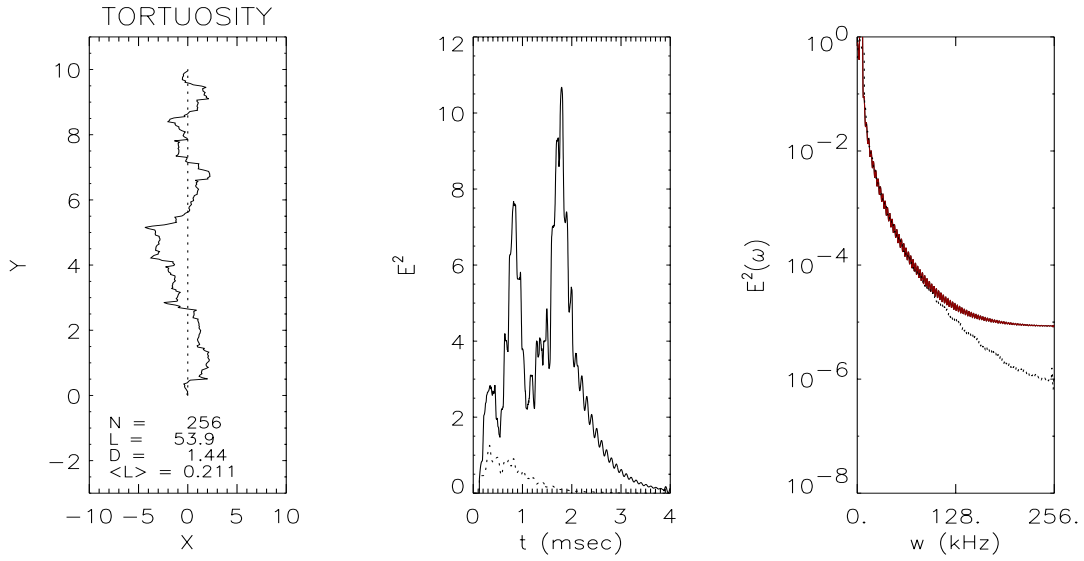

Figure 6: The fractal random walk (a) and its instantaneous radiated power density (b) as well as its power spectrum (c). The dashed lines represent the behavior of the single dipole.

The far field array factor $R = \alpha \int dt \mathbf{E}^2$ (defined in Appendix A) and the

peak power density depend on the path length, or equivalently on the number N of divisions of the fractal. Figure 7b shows the array factor as a function of the path length for the fractal shown in Fig. 7a. Here $n_f = 5$ so that the peak of the array factor is at $a_x = 0$ and $a_y = 0$. There is a clear increase in the array factor from the tortuous fractal as compared with the single dipole.

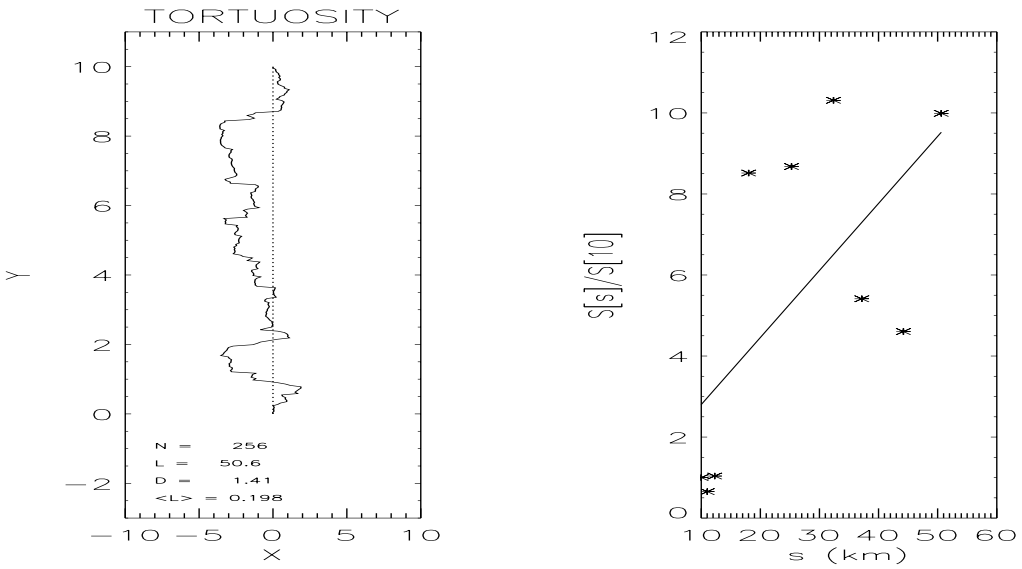

Figure 7: (a) The tortuous discharge. (b) The array factor dependence, normalized to the dipole, on the pathlength.

Therefore, the effect of tortuosity can increase the radiated power density at certain locations as compared to a single dipole antenna.

Another important concept related to fractal antennae is the spatial structure of the radiation field. We can see from the array factor, Eq. (13), that for large n_f $f[\tau, \zeta] \simeq e^{-\tau}(2 + \cos(\zeta\tau))$. The spatial dependence of the array factor will be determined by the factor $\frac{\alpha\zeta\Delta r}{c}$ over the fractal. Consequently, the radiation pattern will have spatial structure when $\frac{\alpha\zeta\Delta r}{c} > 2\pi$, which translate into $n_f > 50$. Figure 8b shows the array factor at the height $h = 60$ km for the discharge structure shown in Fig. 8a with $n_f = 200$. Therefore, such a tortuous fractal can also display a spatial structure in the radiation pattern. But it is more natural for the spatial structure to be generated through a branching process as we will see in the next section.

There is an energy constraint that limits the degree of tortuosity of a fractal lightning discharge since we cannot radiate more energy than what is initially stored as separated charge. Also, if the line elements of the antenna given by Fig. 5 get too close together, then their contribution to the radiated field will tend to cancel each other. Therefore, there is an optimal number of elements forming

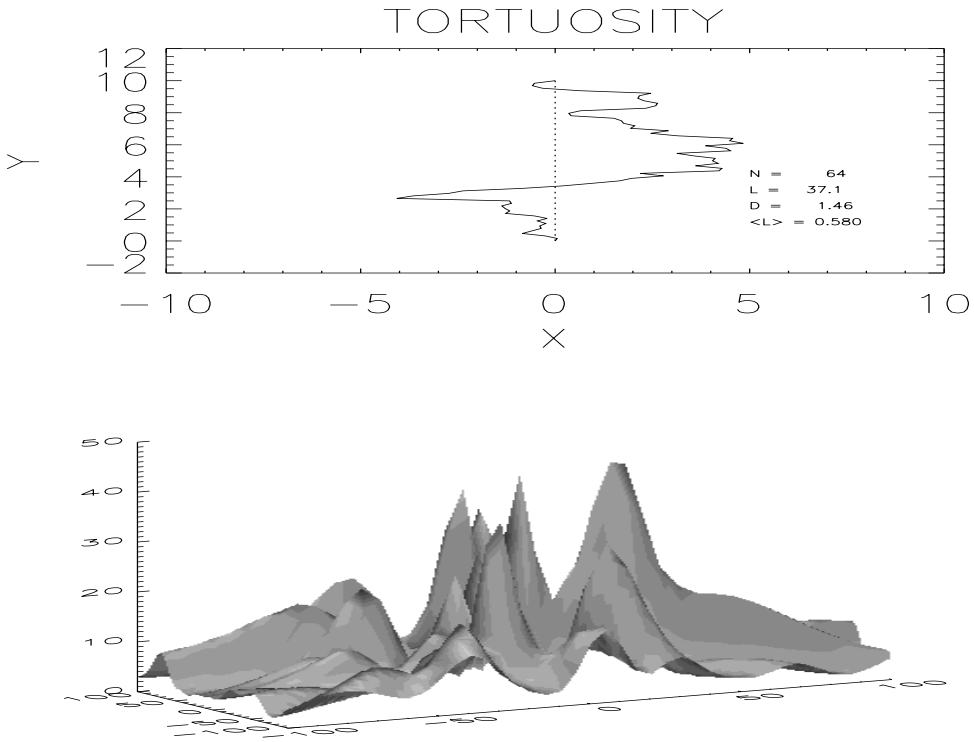

Figure 8: The fractal structure (a) and its array factor(b) showing clear spatial structure in the radiation pattern.

an antenna, and this optimal number translates into an optimal dimension of the fractal, more on this later.

2.3 Branching and Spatial Structure

Another element in understanding fractal antennae is the concept of branching. Take the simple branching element shown in Fig. 9 where the current is divided between the two branching elements. We can compute the radiation field, for a propagating current $\mathrm{I}_o e^{i\omega t}$, as

$$\mathbf{E}(\varepsilon) = \widehat{\mathbf{x}}\frac{\beta(e^{ik\ell a_x}e^{i\frac{k\ell}{\beta}}-1)}{(1-\beta a_x)}+\widehat{\mathbf{y}}\frac{\beta e^{ik\ell a_x}e^{i\frac{k\ell}{\beta}}}{(1-\beta a_y)}\frac{1}{2}\{(e^{ik\ell\varepsilon a_y}e^{i\frac{\varepsilon k\ell}{\beta}}-1)-(e^{-ik\ell\varepsilon a_y}e^{i\frac{\varepsilon k\ell}{\beta}}-1)\}\ldots \tag{6}$$

where $\ell = L/2$ and ε is the variation from the single dipole, i.e. we recover the dipole as $\varepsilon \to 0$.

Again, the analysis can be simplified in the limit for small ε, i.e. $\mathrm{P}(\varepsilon) \simeq \mathrm{P}(0) + \mathrm{P}'(0)\varepsilon + \ldots$. Of course $\mathrm{P}(0)$ is the dipole contribution, and $\mathrm{P}'(0)\varepsilon$

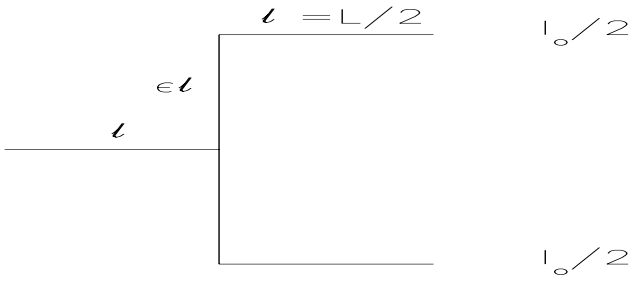

Figure 9: A simple branching situation in which we distribute the current among the branching elements.

is the change in the radiated power density due to the line branching. The dipole has a maximum in the radiated power density $\mathrm{P}(0) \simeq \frac{4\beta^2}{(1-\beta a_x)^2}$, while the branching contribution goes as $\mathrm{P}'(0)\varepsilon \simeq \frac{\beta k L \varepsilon}{(1-\beta a_x)^2}\mathrm{f}(a_x, a_y, kL, \beta, N)$. The function f depends on the given parameters, but its maximum is of the order $\mathrm{f} \sim 1$ with clear regions in (a_x, a_y) where it is positive. Therefore, the branching process can give rise to an increase in the radiated power density at certain position. Of course this increase is due to the increase in the path length. This effect will saturate as ε is increased passed one, since then the strongest contribution will come from the dipole radiator given by $2\varepsilon L$.

A interesting and manageable broadband antenna can be described in terms of the Weierstrass functions [*Werner and Werner*, 1995]. We take successive branching elements, as shown in Fig. 10a, where we distribute the current at each branching point so that the branching element keeps a fraction α of the current. The n^{th} branching element is displaced by a factor ε^n with respect to the origin. If we concentrate only on the contribution from the last branching set, as shown in Fig. 10a, we can write the field as

$$\mathrm{E}_x \sim \sum_{n=1}^{N} \varepsilon^{n(d_o-2)} \cos(kl\varepsilon^n a_y + \phi_n(\beta))$$

$$\phi_n(\beta) = \frac{kl}{\beta}\varepsilon^{n-1}(2+\varepsilon)$$

where we have redefined $\alpha = \varepsilon^{d_o-2}$ and $\mathrm{a}_y = \cos\theta$. In the limit $\beta \to \infty$ and $\mathrm{N} \to \infty$ we obtain the Weierstrass function that is continuous but not differentiable, i.e. is a fractal, and furthermore, its dimension in the sense given by Eq. (1) is d_o. For the purpose of illustration we truncate the above sum to $N = 8$. In Fig. 10b, we show the dependence of the field as a function of $a_y \, \epsilon \, [-1, 1]$ with $\mathrm{a}_x = 0$ for $\beta \to \infty$. The parameters values are shown in the figure caption.

Figure 10c shows the gain factor given by

$$G = \frac{\max |E|^2}{\frac{1}{2}\int da_y \, |E|^2}$$

as a function of the dimension $d_o \, \epsilon \, [0, 1]$. We chose this range since the fractal already has a dimension 1 in the perpendicular directions, i.e. D=1+d_o.

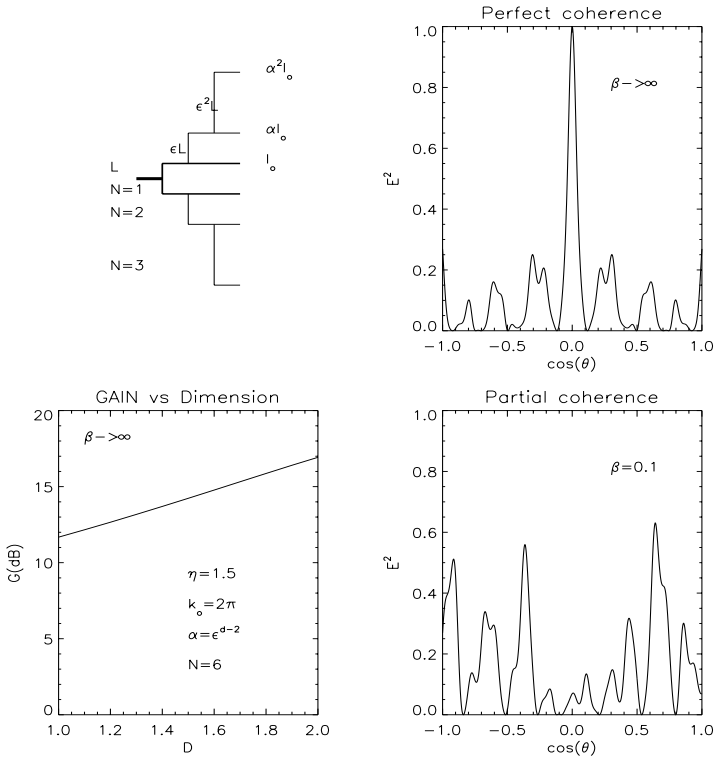

Figure 10: The branching process to produce a Weierstrass radiation pattern. (a) The brunching process with the branching length increasing as $\varepsilon^n L$ and the current decreasing as $\alpha^n I_o$. (b) the radiation pattern with $\beta \to \infty$ given perfect coherence. (c) The gain vs the dimension. It also contains the parameters used in all 3 figures. (d) Patial coherence for $\beta = 0.1$.

Note the increase in the gain as a function of dimension. In general, there is an optimal value of D that generates the highest power density and that does not necessarily has to be for $D = 2$. In Fig. 10b all the elements from the antenna add up coherently at $a_y = 0$, hence providing perfect coherence. For a finite $\beta < 1$ the propagation brings a different phase shift at each element. Figure 10d shows the effect for $\beta = 0.1$ as a function of θ. Note that at no point there is perfect coherence, but there is clear partial coherence. The peak value of E^2 is actually sensitive to β.

Even though fractal antennae naturally lead to the concept of an increase in the peak radiated power, it also has a second important consequence due to branching. As we have seen in the case of the Wiertrauss function, fractal antennae naturally result in the generation of a spatial structure in the radiated power density. This interplay between the spatial structure and the increase in the peak radiated power are the essential ingredients of fractal antennae and why they are so important. A clear example can be illustrated in Fig. 10d where there are multiple relevant peaks of the radiated power in space.

3 Modeling Lightning as a Fractal Antenna

The hypothesis of this work is that the structure of the red sprites can be attributed to the fact that the power density generated by lightning does not have the smooth characteristics expected from the dipole model of Eq. 7, but the structured form expected from a fractal antenna [*Kim and Jaggard*, 1986; *Werner et al.*, 1995]. Previous studies of lightning assumed that the RF fields causing the atmospheric heating and emissions, were produced by an horizontal dipole cloud discharge moment M that generates an electric field at the height z, given by

$$E = \frac{M}{4\pi\epsilon_o z^3} + \frac{1}{4\pi\epsilon_o c z^2}\frac{dM}{dt} + \frac{1}{4\pi\epsilon_o c^2 z}\frac{d^2M}{dt^2} \tag{7}$$

where c is the velocity of light and ϵ_o is the permitivity of free space. It is important to realize that a lightning discharge must be horizontal, as in intracloud lightning, to project the energy upwards into the lower ionosphere. A vertical discharge, as in cloud-to-ground lightning, will radiate its energy horizontally as a vertical antenna.

It is obvious that such a horizontal dipole results in electric fields that vary smoothly with distance. However, it is well known that lightning discharges follow a tortuous path [*LeVine and Meneghini*, 1978]. It was shown [*Williams*, 1988] that intracloud discharges resemble the well known Lichtenberg patterns observed in dielectric breakdown. In fact a time-integrated photograph of a surface leader discharge is illustrated by Figure 11 . These patterns have been recently identified as fractal structures of the Diffusion Limited Aggregate (DLA) type with a fractal dimension $D \approx 1.6$ [*Sander*, 1986; *Niemeyer et al.*, 1984].

As noted previously, the tortuous path increase the effective dipole moment, since now the pathlength along the discharge is longer that the Euclidean distance. To understand this analogy, we construct a tortuous walk between two points separated by a distance R as shown in Fig 12. Take the tortuous path as N small steps of averaged step length $L_o \ll R$, then the total path length S along the tortuous discharge is

$$S \sim NL_o \sim (\frac{R}{L_o})^{D-1}R$$

where the number of small steps is $N \sim (\frac{R}{L_o})^D$ with D as the box counting dimension [*Ott*, 1993]. As we have seen before, the change in the path length

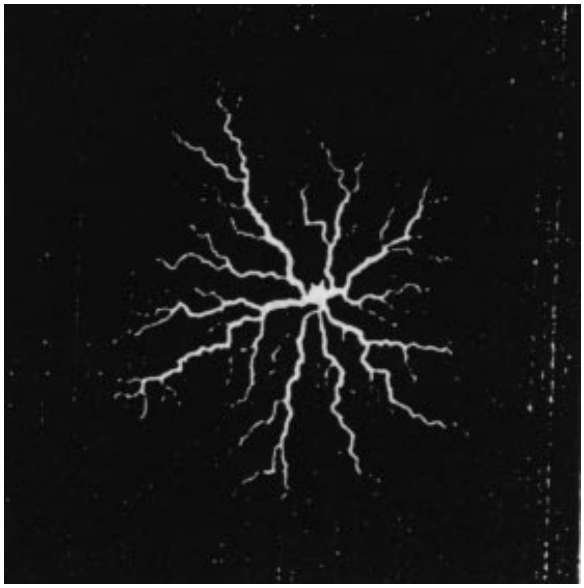

Figure 11: Time-integrated photograph of a surface leader discharge (Lichtenberg pattern) [Niemeyer et al., 1984]

increases the radiated power density as $\mathrm{E}^2 = E_o^2 + \beta k(S-R)$ where $\mathrm{E}_o^2 \sim \beta^2$ Therefore, for $R \sim 10$ km (typical for an intracloud discharge), $L_o \sim 50$ m, $\beta = 0.1$, and $D \sim 1.6$, with obtain $\frac{E^2}{E_o^2} \sim 1 + \frac{kR}{\beta}((\frac{R}{L_o})^{D-1} - 1) \sim 1 + 5f(kHz)$ where f is the frequency of the current.

This is only an analogy, but it gives us good intuition that a fractal lightning discharge will produce an increase in the radiated field intensity, at least locally, as compared with a dipole model and a spatially structured radiation pattern. A fractal dielectric discharge of size R can be modeled as a set of non-uniformly distributed small current line elements [*Niemeyer et al.*, 1984] that represent the steps of the discharge breakdown as it propagates during an intracloud lightning discharge. The size of the elementary current steps is about $L_o \sim 50$ m [*Uman*, 1987]. As a current pulse propagates along this horizontal fractal discharge pattern it radiates energy upwards (see Appendix A on how the fields are calculated) as well as downward.

To determine the extent over which the non-uniformity of the lightning discharge current affects the power density structure projected in the lower ionosphere, we will now construct a simple fractal model of the lightning discharge that will yield a spatio-temporal radiation pattern at the relevant heights.

3.1 Fractal Lightning: Stochastic Model

We want to generate a fractal model that can be parametrized by its fractal dimension. For this purpose, we follow *Niemeyer et al.* [1984] who proposed a two

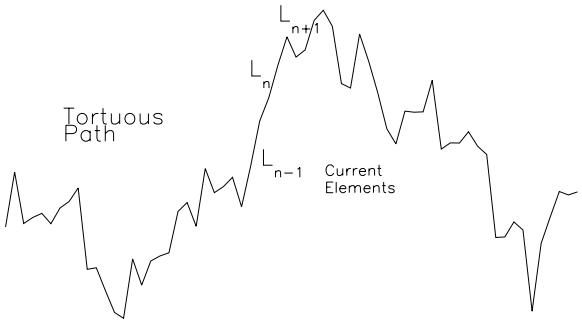

Figure 12: Tortuous path between two point.

dimensional stochastic dielectric discharge model that naturally leads to fractal structures. In this model the fractal dimension D can be easily parametrized by a parameter η. Femia et al. [1993] found experimentally that the propagating stochastic Lichtenberg pattern is approximately an equipotential. Then, the idea is to create a discrete discharge pattern that grows stepwise by adding an adjacent grid point to the discharge pattern generating a new bond. The new grid point, being part of the discharge structure, will have the same potential as the discharge pattern. Such local change will affect the global potential configuration, see Fig. 13.

The potential for the points not on the discharge structure is calculated by iterating the discrete two dimensional Laplace's equation

$$\nabla^2 \phi = 0$$
$$\phi_{i,j} = \tfrac{1}{4}(\phi_{i+1,j} + \phi_{i-1,j} + \phi_{i,j+1} + \phi_{i,j-1})$$

until it converges. This method reproduces the global influence of a given discharge pattern as it expands. The discharge pattern evolves by adding an adjacent grid point. The main assumption here is that an adjacent grid point denoted by (l,m) has a probability of becoming part of the discharge pattern proportional to the η power of the local electric field, which translates to

$$p(i,j) = \frac{\phi_{i,j}^{\eta}}{\sum_{l,m} \phi_{l,m}^{\eta}}$$

in terms of the local potential. Here we have assumed that the potential at the discharge is zero. The structure generated for $\eta = 1$, corresponding to a Lichtenberg pattern, is shown in Fig. 14.

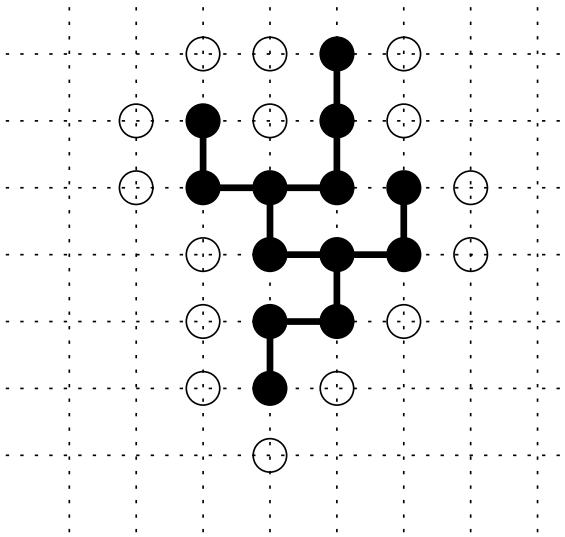

Figure 13: Diagram of the discrete discharge model.

The color coding corresponds to the potential. Figure 15 shows a plot of $N(\varepsilon)$ vs. $Log(\varepsilon)$ for the fractal discharge of Fig. 14, i.e. $\eta = 1.0$. Again the scaling behavior only occurs over a few decades, but it is very clear. The dimension of this structure is $D \simeq 1.6$.

Note that this model, and also the dimension of the discharge, is parametrized by η. Intuitively we expect that when $\eta = 0$ the discharge will have the same probability of propagating in any direction, therefore, the discharge will be a compact structure with a dimension $D = 2$. If $\eta \to \infty$ then the discharge will go in only one direction, hence $D = 1$. Between these two limits, the dimension will be the function $D(\eta)$ shown in Fig 16. As an example the corresponding structure generated for $\eta = 3$ (Fig 17) has a dimension of $D = 1.2$.

To compute the radiated fields, we must describe the current along each of the segments of the fractal discharge. We start with a charge Q_o at the center of the discharge. The current is then discharged along each of the dendritic arms. At each branching point we chose to ensure conservation of current, but intuitively we know that a larger fraction of the current will propagate along the longest arm. Suppose that a current I_o arrives at a branching point, and if L_i is the longest distance along the i^{th} branching arm, we intuitively expect that the current on the i^{th} arm should be proportional to L_i^η. Therefore, we satisfy charge (or current) conservation if the current along the i^{th} branching arm is

$$I_i = \frac{L_i^\eta}{\sum_j L_j^\eta}$$

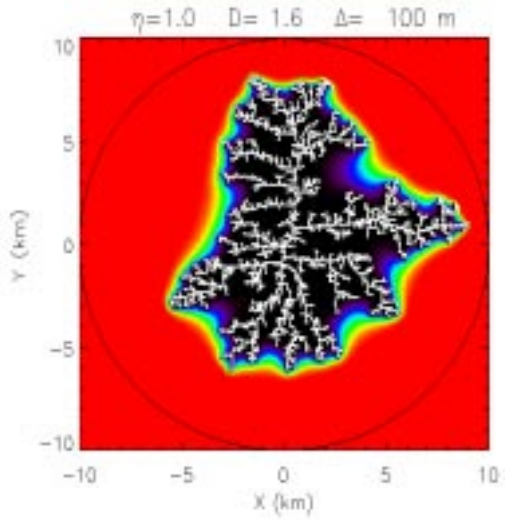

Figure 14: Fractal discharge generated with $\eta = 1$.

3.2 Computing the Fields from the Fractal Structure

A current pulse propagates along the horizontal (in the x-y plane) 2 dimensional fractal discharge structure, e.g. $I(x,t) = I(t - \frac{s}{v})$ generating radiation fields. The radiation field is the superposition, with the respective phases, of the small line current elements. The intracloud current pulse is taken as a series of train pulses that propagate along the arms of the antenna

$$I(t) = I_o(e^{-\alpha t} - e^{-\gamma t})(1 + \cos(\omega t))\theta(t)$$

with $\omega = 2\pi\alpha n_f$ and $\theta(t)$ as the step function. Here n_f represent the number of oscillations during the decay time scale $1/\alpha$. We chose the decay parameters as $\alpha = 10^3$ s^{-1} and $\gamma = 2 \times 10^5$ s^{-1}, hence $\gamma/\alpha = 200$, which correspond to realistic parameters for lightning [*Uman*, 1987]. The total charge discharged is then $Q = I_o/\alpha$, which for $I_o = 100\,kA$ gives $Q \sim 100\,C$. As we have seen before, we require $n_f \sim 100$ to create the spatial structures so that the exponential decay $e^{-\alpha t}$ can be considered as the envelope of the oscillating part.

On a given position the time dependence of the field intensity E^2 has a fractal structure, as it is shown in Fig. 18a for the stochastic discharge model with $\eta = 3$. The frequency spectrum of the electric field is shown in Fig. 18b. It is very important to realize that the relevant frequencies are below a few hundred kHz. By restricting the field frequencies to below a few hundred kHz, the analysis is greatly simplified, since then the conductivity and dielectric tensors can be considered as independent of time in the lower ionosphere (see Appendix B).

The large conductivity of the ground at these frequencies can be included by assuming to first order an image discharge of opposite current below a perfectly

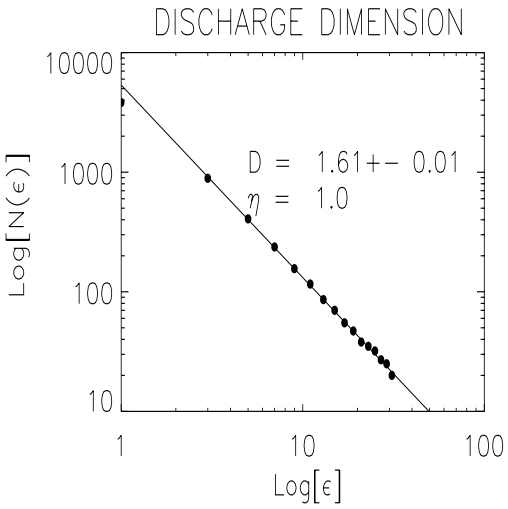

Figure 15: The plot of $lnN(\epsilon)$ vs $\frac{1}{\epsilon}$ for $\eta = 1$.

conductive plane. The primary discharge is taken to be at $z_o = 5$ km above the ground. This parameter is not very relevant, since we are interested in the field at heights of about $h \sim 80$ km, therefore, moving the discharge from 5 to 10 km will only change the field strength by a marginal 10%.

3.3 How does the Fractal Dimension Affect the Field Pattern?

For a 2-dimensional fractal structure, we expect that the strength of the radiated power density depends on the fractal structure, i.e. its fractal dimension. If the strength of the k Fourier component is A_k then the field in the far field [*Jackson* 1975] at r along the axis of the fractal will be given by

$$\mathbf{E} \sim \int dk A_k \int_\mu d\mu \mathbf{R}(\mu) \sin(k\rho)$$

where dμ (the fractal measure) is the contribution of the fractal from a given polar position (ρ,ϕ). $\mathbf{R}(\mu)$ is the phase contribution from the elements of the fractal at position (ρ,ϕ) and in the far field should be proportional to the direction of the local current. Note that a radially propagating uniform 2 dimensional current structure will generate no field at the axis since contributions to $\mathbf{R}(\mu)$ from different parts of the fractal will cancel each other.

The cross section of the fractal at a given radius ρ will resemble a Cantor set in $\phi \in [0, 2\pi]$, and the phase contribution will be given by $\mathbf{S}(\rho) = \int_\mu d\phi \mathbf{R}(\rho, \phi)$ which will be finite for an asymmetrical fractal. The integration can be carried as a Lebesgue integral or as a Riemann-Stieltjes integral over this pseudo-Cantor

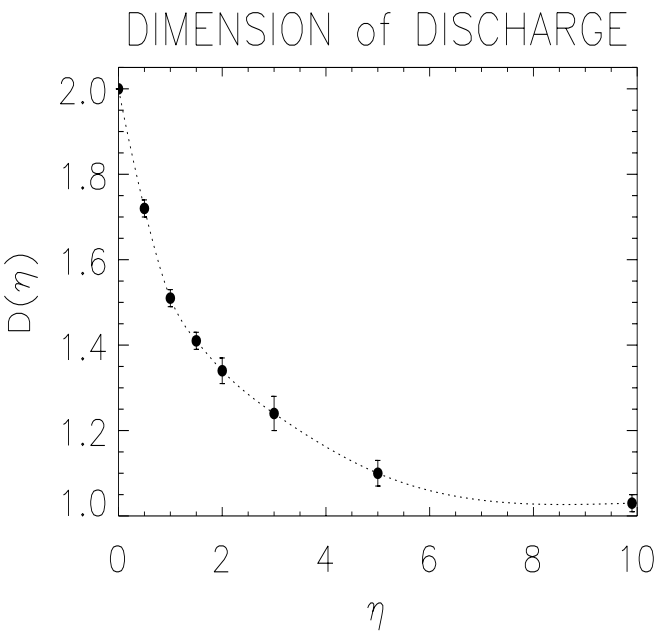

Figure 16: The dimension of the stochastic model as a function of η with the estimated error bars.

set [*Royden*, 1963]. Note that if the fractal is uniformly distributed along ϕ, corresponding to D=2, then $\mathbf{S}(\rho) = 0$. Similarly, for a delta function at $\phi = \phi_o$ corresponding to D=1, $\mathbf{S}(\rho)$ gives a positive contribution. $\mathbf{S}(\rho)$ is a very complicated function that depends on the details of the current distribution along the fractal. In an average sense we can suppose that $S(\rho) \sim f(D)$ where $f(D = 1) = 1$ and $f(D = 2) = 0$ but f can be greater than one for other values as has been investigated in previous sections when branching and propagation occurs. Therefore,

$$E \sim f(D) \int dk\, A_k \int_\mu dm(\rho)\; I(\rho) \sin(k\rho)$$

where dm(ρ) represents the amount of the fractal between ρ and $\rho + d\rho$ and I(ρ) is the averaged current over ϕ at radius ρ. A fractal will have a mass up to a radius ρ given by $m(\rho) = (\frac{\rho}{L_o})^D$ by noting that a 2 dimensional antenna will have more elements than a one dimensional fractal. In general, due to the branching process, some of the current does not reach the radius R. But for simplicity, if all of the current reaches the end of the fractal at radius R, then $dm(\rho)\; I(\rho) = d\rho$. In such case, the above integral gives

$$E \sim f(D) \int dk\; k^{-1} A_k (1 - \cos(kR))$$

Note that $\varepsilon = (\frac{\ell}{R})$ in some sense selects the Fourier component $k = \frac{2\pi\beta}{\varepsilon R}$ which has a strength $A_k \sim N(\varepsilon) \sim \varepsilon^{-D}$. The integral over k gives $g(D) \simeq (\frac{L_o}{R})^{D-1}$, therefore, the field is given by

$$E \sim f(D)g(D) \tag{8}$$

which shows that the field has a maximum value at a specific value of $D \epsilon [1, 2]$ since $f(D)$ decreases and $g(D)$ increases with D respectively.

On the other hand, the Rayleigh length, the distance beyond which the field start decaying to their far field values, behaves as $R_L(\varepsilon) \sim \frac{\varepsilon R}{2\pi\beta}$ for a given ε. Red sprites occur at a height $z \sim 80$ km, therefore, for $z > R_L(\varepsilon)$, elements with sizes smaller than ε do not contribute to the field, i.e. as we increase z we wash out the information of increasingly larger spatial scales of the fractal. It is the power law dependence, as specified by the fractal dimension, that determine the field pattern.

Even though, the radiation pattern will depend on the details of the fractal structure, we expect that the most relevant parameter in determining the radiation pattern will be the fractal dimension, as found by Myers et al. [1990] for simple fractals. There is an interplay between the dimension and the spatial structure of the radiation pattern. For a dimension close to $D \sim 1$or $D \sim 2$, there will be no significant spatial structure. While an intermediate dimension can produce a significant spatial structure.

3.4 Fields from the Stochastic Model

First we start by computing the array factor based on the far field approximation (see Appendix A). We take $\mathrm{n}_f \sim 200$ and $\beta = 0.1$ and compute the array factor at a height $z = 60$ km. Figure 19 shows the array factor for the discharge structure shown in Fig. 17 with $\eta = 3$.

The length of the elementary current elements is about 100 m. The array factor shows clear structure. A cross-section of the normalized array factor are shown in Fig. 20 and Fig. 21 for $\eta = 1$ and $\eta = 2$ respectively.

Similarly, the array factor at $x = 10$ km, $y = 10$ km, $z = 60$ km is shown as a function of the fractal dimension of the discharges for $\beta = 0.05$ and $\beta = 0.025$ in Fig. 22a for $\mathrm{n}_f = 0$ and Fig. 22b for $\mathrm{n}_f = 200$.

The fractal dimension dependence of the array factor is very intriguing, but is of clear significance for our lightning studies. What about the time dependence of the radiations fields? Figure 23 shows the time dependence of the radiation fields for $\eta = 1, 2, 3, 5, 10$ with $\mathrm{n}_f = 200, 50, 1$ where each figure is carefully labeled. Again the relevance of the $\eta = 3$ case is very striking. Each column of graphs represent the time dependence for $\mathrm{n}_f = 200, 50, 1$ respectively, where the rows represent the case for $\eta = 1, 2, 3, 5, 10$. The amplitude of the field has been multiplied by the factor displayed next to the graph.

We take the case for $\eta = 3$ and we study the dependence of the array factor as a function of the current frequency as parametrized by n_f. Figure 24 shows the frequency dependence of the array factor at this location $x = 10$ km, $y = 10$

km, $z = 60$ km. Initially the array factor increases linearly with n_f as expected but then it starts to oscillate as the spatial variation of the field pattern becomes relevant.

In conclusion, the fractal nature of the discharges, being a simple random walk or a stochastic discharge model, leads naturally to an increase in the peak power density as compared with the dipole model. This increase is related to the increase in the antenna path length, or tortuosity, and on the branching process. It will be shown later that this gain in peak power density leads to a significant reductions in the discharge properties (e.g. charge, peak current) required to produce the observed sprite emissions. Furthermore, if the discharge has a high frequency component, as expected from an acceleration and deceleration process in each of the single steps, then the radiation pattern can show spatial structure. This spatial structure of the lightning induced radiation pattern will be related to the spatial structure of the red sprites in the next chapter.

4 Appendix A: Fields from a Fractal Structure

The fields from a line element can be solve with the help of the Hertz Vector [*Marion and Heald*, 1980]. In order to solve Maxwell's equations we define, in empty space, the vector function $\mathbf{Q}$ [*Marion and Heald*, 1980] that is related to the current density $\mathbf{J}$ and the charge density ρ as

$$\mathbf{J} = -\frac{\partial \mathbf{Q}}{\partial t}$$

$$\rho = \nabla \cdot \mathbf{Q}$$

Note that $\mathbf{Q}$ solves the continuity equation trivially, and furthermore, it can be used to define another vector function, namely the Hertz vector $\mathbf{\Pi}(\mathbf{x}, t)$, as

$$\nabla^2 \mathbf{\Pi} - \frac{1}{c^2}\frac{\partial^2 \mathbf{\Pi}}{\partial t^2} = -4\pi \mathbf{Q}$$

where the fields are then defined as

$$\mathbf{B}(\mathbf{x}, t) = \frac{1}{c}\nabla \times \frac{\partial \mathbf{\Pi}(\mathbf{x}, t)}{\partial t}$$

$$\mathbf{E}(\mathbf{x}, t) = \nabla \times \nabla \times \mathbf{\Pi}(\mathbf{x}, t)$$

The time-Fourier transformed Maxwell's equations, with $\mathbf{Q}(\mathbf{x}, \omega) = \frac{i}{\omega}\mathbf{J}(\mathbf{x}, \omega)$ and $\mathbf{J}(\mathbf{x}, \omega) = \widehat{\mathbf{L}}\mathrm{I}(l, \omega)$, can be solved with the help of the Hertz vector $\mathbf{\Pi}$,

$$\mathbf{\Pi}(\mathbf{x}, \omega) = \frac{i}{\omega}\int_0^L \mathbf{J}(l, \omega)\frac{e^{ik\left\|\mathbf{x} - l\widehat{\mathbf{L}}\right\|}}{\left\|\mathbf{x} - l\widehat{\mathbf{L}}\right\|}dl \tag{9}$$

where the line element has orientation $\mathbf{L}$ and length L, and is parametrized by $l \in [0, L]$. Values with the hat $\widehat{\ }$ indicate unit vectors, variables in bold indicate vectors, ω is the frequency, $k = \frac{\omega}{c}$. The time dependence can be found by inverting the above equation.

4.1 Fields from a Fractal Antennae

A current pulse propagates with speed $\beta = \frac{v}{c}$ along a fractal structure. At the n^{th} line element with orientation $\mathbf{L}_n$ and length L_n, which is parametrized by $l \,\epsilon\, [0, L_n]$, the current is given by $I(l, s_n, t) = I_o(t - \frac{s_n + l}{v})$ where s_n is the path length along the fractal (or if you prefer a phase shift). The radiation field is the superposition, with the respective phases, of the small line current elements that form the fractal. For a set $\{\mathbf{r}_n, \mathbf{L}_n, I(s_n, t) \,|\, n = 0, ..., N\}$ of line elements, such as shown in the example diagram of Fig. 25, the Hertz vector is given by

$$\mathbf{\Pi}(\mathbf{x}, \omega) = \sum_{\{n\}} \widehat{\mathbf{L}}_n \frac{i}{\omega} \int_0^{L_n} \mathrm{I}_o(\omega) e^{i\frac{\omega}{v}(s_n + l)} \frac{e^{ik\|\mathbf{r}_n - l\widehat{\mathbf{L}}_n\|}}{\| \mathbf{r}_n - l\widehat{\mathbf{L}}_n \|} dl \tag{10}$$

where $\mathbf{r}_n$ is the vector from the beginning of the n^{th} line element to the field position $\mathbf{x}$, ω is the frequency and $k = \frac{\omega}{c}$.

We must realize that in general Eq. 10 for $\mathbf{\Pi}$ is very complicated, but we are interested in the far field of the small line elements ($r_n \gg L$). Therefore, we can take the far field approximation of the small line elements to obtain a closed form solution for the Fourier transformed fields as

$$\mathbf{B}(\mathbf{x}, \omega) = -\sum_{\{n\}} \frac{k^2 e^{ikr_n}}{r_n} f(s_n, \omega, r_n)[1 + \frac{i}{(kr_n)}](\widehat{\mathbf{L}}_n \times \widehat{\mathbf{r}}_n)$$

$$\begin{aligned}\mathbf{E}(\mathbf{x}, \omega) = -\textstyle\sum_{\{n\}} \frac{k^2 e^{ikr_n}}{r_n} f(s_n, \omega, r_n)[(1 + \frac{i}{(kr_n)} + \frac{i^2}{(kr_n)^2})\widehat{\mathbf{L}}_n \\ -\widehat{\mathbf{r}}_n(\widehat{\mathbf{L}}_n \cdot \widehat{\mathbf{r}}_n)(1 + \frac{3i}{(kr_n)} + \frac{3i^2}{(kr_n)^2}]\end{aligned}$$

where the geometric factor is given by

$$f(s_n, \omega, r_n) = \frac{i}{\omega} \int_0^{L_n} I_o(s_n, l, \omega) e^{-i(\widehat{\mathbf{L}}_n \cdot \widehat{\mathbf{r}}_n)kl} dl = \frac{ie^{i\frac{c}{v}s_n}}{\omega} I_o(\omega) \int_0^{L_n} e^{i(\frac{c}{v} - (\widehat{\mathbf{L}}_n \cdot \widehat{\mathbf{r}}_n)k)l} dl$$

$$f(s_n, \omega, r_n) = \frac{\beta I_o(\omega) e^{i\frac{\omega}{v}s_n}}{ck^2(1 - \beta(\widehat{\mathbf{L}}_n \cdot \widehat{\mathbf{r}}_n))}(1 - e^{i(\frac{c}{v} - (\widehat{\mathbf{L}}_n \cdot \widehat{\mathbf{r}}_n)k)L_n})$$

Note that even though we are in the far field of the small line elements, we can be in fact in the intermediate field with respect to the global fractal structure. Therefore, phase correlations over the fractal can be extremely relevant, and produce spatially nonuniform radiation fields. We then invert the Fourier transform of the field to real time and obtain the spatio-temporal radiation pattern due to the fractal discharge structure

$$\mathbf{B}(\mathbf{x}, t) = \sum_{\{n\}} \frac{-(\widehat{\mathbf{L}}_n \times \widehat{\mathbf{r}}_n)}{cr_n(\frac{c}{v} - (\widehat{\mathbf{L}}_n \cdot \widehat{\mathbf{r}}_n))}[I_o(\tau) \,|_{t-\tau_2}^{t-\tau_1} + \frac{c}{r_n} I_1(\tau) \,|_{t-\tau_2}^{t-\tau_1}]$$

$$\begin{aligned}\mathbf{E}(\mathbf{x}, t) = \textstyle\sum_{\{n\}} \frac{1}{cr_n(\frac{c}{v} - (\widehat{\mathbf{L}}_n \cdot \widehat{\mathbf{r}}_n))}[(I_o(\tau) \,|_{t-\tau_2}^{t-\tau_1} + \frac{c}{r_n} I_1(\tau) \,|_{t-\tau_2}^{t-\tau_1} + \frac{c^2}{r_n^2} I_2(\tau) \,|_{t-\tau_2}^{t-\tau_1})\widehat{\mathbf{L}}_n - \\ \widehat{\mathbf{r}}_n(\widehat{\mathbf{L}}_n \cdot \widehat{\mathbf{r}}_n)(I_o(\tau) \,|_{t-\tau_2}^{t-\tau_1} + \frac{3c}{r_n} I_1(\tau) \,|_{t-\tau_2}^{t-\tau_1} + \frac{3c^2}{r_n^2} I_2(\tau) \,|_{t-\tau_2}^{t-\tau_1})]\end{aligned} \tag{11}$$

where

$$I_1(t) = \int_{-\infty}^{t} d\tau I_o(\tau)$$

$$I_2(t) = \int_{-\infty}^{t} d\tau \int_{-\infty}^{\tau} d\tau^{'} I_o(\tau^{'})$$

can be calculated exactly for the current described above, and where

$$\tau_1 = \frac{r_n}{c} + \frac{s_n}{\mathrm{v}}$$

$$\tau_2 = \frac{r_n + (\widehat{\mathbf{L}}_n \cdot \widehat{\mathbf{r}}_n) L_n}{c} + \frac{s_n + L_n}{\mathrm{v}} + (\widehat{\mathbf{L}}_n \cdot \widehat{\mathbf{r}}_n) \frac{L_n}{c}$$

The value of τ_1 and τ_2 correspond to the causal time delays from the two end points of the line element.

Before finishing this section we want to mention that there is an inherent symmetry in the radiation fields. In general we will assume that the current is given by $I(t) = I_o e^{-\alpha t}(1 - \cos(2\pi n \alpha t))\theta(t)$ where $\theta(t)$ is the step function, and $n \geq 1$. Note that the total charge discharged by this current is Q=I_o/α where $1/\alpha$ is the decay time of the current. But since the current propagates along the fractal, the radiation fields at a given position in space will last for a time given by $\tau = \frac{s}{\mathrm{v}} + \alpha$ where s is the largest path length along the fractal. The fields are invariant as long as αt , $\frac{L\alpha}{\mathrm{v}}$ and $\mathbf{r}\alpha$ are kept constant in the transformation. Such scaling can become relevant in studying the properties of radiation fields from fractal antennae.

In general we will use the power density $S(W/m^2) = c\varepsilon_o E^2(V/m)$, where $1/c\varepsilon_o$ is the impedance of free space, as a natural description for the amount of power radiated through a cross-sectional area.

4.2 The Far field

The far field is approximately given by

$$\mathbf{E}(\mathbf{x}, t) = \sum_{\{n\}} \frac{\beta I_o(\tau) \mid_{t-\tau_2}^{t-\tau_1}}{c r_n (1 - \beta(\widehat{\mathbf{L}}_n \cdot \widehat{\mathbf{r}}_n))} \tag{12}$$

In general we are going to use a current pulse defined as $I(t) = I_o(e^{-\alpha t} - e^{-\gamma t})(1 + \cos(\omega t))\theta(t)$ with $\omega = 2\pi\alpha n_f$ and $\theta(t)$ as the step function. Here n_f represent the number of oscillations during the decay time scale $1/\alpha$. We chose the decay parameters as $\alpha = 10^3$ s^{-1} and $\gamma = 2 \times 10^5$ s^{-1}, hence $\gamma/\alpha = 200$, which correspond to realistic parameters for lightning [*Uman*, 1987].

As a measure of the amount of energy radiated to a given point in the far field, we can define an array factor as $R(x, y, z) \sim \alpha \int E^2 dt$. From Eq. (12) we can write this array factor as

$$R \simeq \frac{\beta^2 \zeta^2}{4(4 + 5\zeta^2 + \zeta^4)} \sum_{n,m} \frac{\widehat{\mathbf{L}}_n \cdot \widehat{\mathbf{L}}_m \, \mathrm{I}_n \mathrm{I}_m}{(1 - \beta a_n)(1 - \beta a_m) r_n r_m} \{ f[\left|\tau_n^f - \tau_m^f\right|, \zeta] +$$

$$f[\left|\tau_n^i - \tau_m^i\right|, \zeta] - f[\left|\tau_n^f - \tau_m^i\right|, \zeta] - f[\left|\tau_n^i - \tau_m^f\right|, \zeta]\} \tag{13}$$

$$f[\tau, \zeta] = e^{-\tau}[2 + 2\zeta^2 + (\zeta^2 - 2)\cos(\zeta\tau) + 3\zeta\sin(\zeta\tau)]$$

where $\tau_n^i = \alpha(\frac{r_n}{c} + \frac{s_n}{\mathrm{v}})$ corresponds to the parameters from the beginning (i) of the line element, and similarly for the endpoint (f). Also $\zeta = 2\pi n_f$ and I_n is the current strength of the n^{th} element. The array factor can be normalized by maximum in the array factor corresponding to the single dipole, i.e.,

$$R_o \simeq \frac{\beta^2 \mathrm{I}_o^2 \, A}{4(1-\beta a)^2 h^2}$$

where $A = \{\frac{3\zeta^4 - \zeta^2 f[\frac{1}{\alpha \mathrm{v}}(\beta\Delta r - L), \zeta]}{2(4+5\zeta^2+\zeta^4)}\} \simeq 1$, with $\Delta r \simeq L\widehat{\mathbf{x}} \cdot \widehat{\mathbf{r}}$ as the difference in distance between the beginning and end points of the dipole to the detector position. h is the height of the detector.

References

[1] Atten, P., A. Saker, *IEEE Trans. Electr. Insulation*, 28, 230, 1993.

[2] Bell, T. F., V. P. Pasko, and U. S. Inan, Runaway electrons as a source of Red Sprites in the mesosphere, *Geophys. Res. Lett.*, 22, 2127–2130, 1995.

[3] Bethe, H. A., and J. Ashkin, Passage of radiations through matter, in *Experimental Nuclear Physics* (ed. E. Segre) Wiley, New York 1953, pp. 166–357.

[4] Boeck, W. L., O. H. Vaughan, Jr., R. Blakeslee, B. Vonnegut, and M. Brook, Lightning induced brightening in the airglow layer, *Geophys. Res. Letts.*, 19(2), 99–102, 1992.

[5] Bossipio, D. J., E. R. Williams, S. Heckman, W. A. Lions, I. T. Baker, and R. Boldi, Sprites, ELF transients, and positive ground strokes, *Science*, 269, 1088–1091, 1995.

[6] Brasseur, G., and S. Solomon, Aeronomy of the Middle Atmosphere, D. Reidel, Norwell, Mass., 1984.

[7] Cartwright, D. C, Total Cross Sections for the Excitation of the Triplet States in Molecular Nitrogen, *Phys. Rev., A2*, 1331–1347, 1970.

[8] Cartwright, D. C, S. Trajamar, A. Chutjian, and W. Williams, Electron impact excitation of the electronic states of N2. II. Integral cross sections at incident energies from 10 to 50 eV, *Phys. Rev., A*16, 1041–1051, 1977.

[9] Cartwright, D. C., Vibrational Populations of the Excited States of N2 Under Auroral Conditions, *J. Geophys. Res.*, A83, 517–531, 1978.

[10] Connor, J. W., and R. J. Hastie, Relativistic limitation on runaway electrons, *Nucl. Fusion*, 15, 415–424, 1975.

[11] Daniel, R. R., and S. A. Stephens, Cosmic-ray-produced electrons and gamma rays in the atmosphere, *Rev. Geophys. Space Sci.*, 12, 233–258, 1974.

[12] Dreicer, H., Electron and ion runaway in a fully ionized gas. II, *Phys. Rev.*, 117, 329–342, 1960.

[13] Farrel, W. M., and M. D. Desch, Cloud-to-stratosphere lightning discharges: a radio emission model, *Geophys. Res. Lett.*, 19(7), 665–668, 1992.

[14] Farrel, W. M., and M. D. Desch, Reply to comment on "Cloud-to-stratosphere lightning discharges: a radio emission model", *Geophys. Res. Lett.*, 20(8), 763–764, 1993.

[15] Femia, H., L. Niemeyer, V. Tucci, Fractal Characteristics of electrical discharges: experiments and simulations, *J. Phys. D: Appl. Phys.*, 26, p. 619, 1993.

[16] Fishman, G. J., P. N. Bhat, R. Mallozzi, et al., Discovery of intense gamma-ray flashes of atmospheric origin, *Science*, 264, 1313–1316, 1994.

[17] Franz, R. C., R. J. Memzek, and J. R. Winckler, Television image of a large upward electrical discharge above a thunderstorm system, *Science*, 249, 48–51, 1990.

[18] Freund, R. S., Electron Impact and Excitation Functions for the and States of N2, *J. Chem. Phys.*, 54, 1407-1409, 1971.

[19] Gilmore, F. R., R. R. Laher, and P. J. Espy, Franck-Condon factors, r-centroids, electronic transition moments, and Einstein coefficients for many nitrogen and oxygen systems, *J. Phys. Chem.* Ref. Data, 21, 1005–1067, 1992.

[20] Goodman, J. W., *Statistical Optics*, Wiley-interscience, 1985.

[21] Greenblatt, G. D., J. J. Orlando, J. B. Burkholder and A. R. Ravishankara, Absorption Measurements of Oxygen between 330 and 1140 nm, *J. Geophys. Res.*, 95, 18,577–18,582, 1990.

[22] Gurevich, On the theory of runaway electrons, *JETP*, 39, 1996–2002, 1960; *Sov. Phys. JETP*, 12, 904–912, 1961.

[23] Gurevich, A. V., *Nonlinear phenomena in the Ionosphere*, Springer, 1978

[24] Gurevich A. V., G. M. Milikh, and R. Roussel-Dupre, Runaway electrons mechanism of the air breakdown and preconditioning during thunderstorm, *Phys. Lett. A*, 165, 463, 1992.

[25] Gurevich A. V., G. M. Milikh, and R. Roussel-Dupre, Nonuniform runaway breakdown, *Phys. Lett. A*, 187, 197, 1994.

[26] Gurevich, A. V., J. A. Valdivia, G. M. Milikh, K. Papadopoulos, Runaway electrons in the atmosphere in the presence of a mangetic field, *Radio Science*, 31, 6, p. 1541, 1996.

[27] Hale, L. C., and M. E. Baginski, Current to the ionosphere following a lightning stroke, *Nature*, 329, 814–816, 1987.

[28] Hampton, D. L., M. J. Heavner, E. M. Wescott, and D. D. Sentman, Optical spectral characteristics of sprites, *Geophys. Res. Lett.*, 23, 89–92, 1996.

[29] *Handbook of Chemistry and Physics*, 64–th Edition, Ed. R. C. Weast, CRC Press, Boca Raton, Florida, 1983–1984.

[30] *Handbook of Geophysics and Space Environment*, 64–th Edition, Ed. A. S. Jursa, Air Force Geophysics Laboratory, US Air Force, 1985.

[31] Huang, K., *Statistical Mechanics*, Wiley, 1987.

[32] Jackson, J. D., *Classical Electrodynamics*, Wiley, 1975.

[33] Jaggard, D. L., On fractal electrodynamics, In *Recent Advancements in Electromagnetic Theory*, edited by H. N. Kritikos and D. L. Jaggard, p. 183, Springer-Verlag, New York, 1990.

[34] Kerr, R. A., Atmospheric scientists puzzle over high-altitude flashes, *Science*, 264, 1250–1251, 1994.

[35] Kim, Y., and D. L. Jaggard, The fractal random array, *Proceedings of the IEEE*, 74, 1986.

[36] Krider, E. P., On the electromagnetic fields, pointing vector, and peak power radiated by lightning return strokes, *J. Geophys. Res.*, 97, 15913–15917, 1992.

[37] Krider, E. P., On the peak electromagnetic fields radiated by lightning return strokes toward the middle atmosphere, *J. Atmos. Electr.*, 14, 17–24, 1994.

[38] Le Vine, D. M., and R. Meneghini, Simulations of radiation from lightning return strokes: the effects of tortuosity *Radio Science*, 13, 801–810, 1978.

[39] Lebedev, A. N., Contribution to the theory of runaway electrons, *Sov. Phys. JETP*, 21, 931–933, 1965.

[40] Lenoble, J., *Atmospheric Radiative Transfer*, A. Deepak Publishing, Hampton, Virginia, 1993

[41] Longmire, C. L., On the electromagnetic pulse produced by nuclear expulsion, *IEEE Trans. Antenna Propag.*, 26, 3–13, 1978.

[42] Luther, F. M., and R. J. Gelinas, Effect of molecular multiple scattering and surface albedo on atmosphere photodissociation rate, *J. Geophys. Res.*, 81, 1125–1138, 1976.

[43] Lyons, W. A., Characteristics of luminous structures in the stratosphere above thunderstorms as imaged by low-light video, *Geophys. Res. Lett.*, 21, 875–878, 1994.

[44] Lyons, W. A., Sprite observations above the U.S. High Plains in relation to their parent thunderstorm systems, *J. Geophys. Res.*, 101, D23, 29641-29652, 1996.

[45] Marion, J. B., M. A. Heald, Classical Electromagnetic Radiation, Harcourt Brace Jovanovich, 1980.

[46] McCarthy, M. P., and G. K. Parks, Om the modulation of X-ray fluxes in thunderstorms, *J. Geophys. Res.*, 97, 5857–5864, 1992.

[47] Massey, R. S., and D. N. Holden, Phenomenology of trans-ionoispheric pulse pairs, *Radio Science*, 30(5), 1645, 1995.

[48] Mende, S. B., R. L. Rairden, G. R. Swenson and W. A. Lyons, Sprite Spectra; N2 1 PG Band Identification, *Geophys. Res. Lett.*, 22, 1633–2636, 1995.

[49] Milikh, G. M., K. Papadopoulos, and C. L. Chang, On the physics of high altitude lightning, *Geophys. Res. Lett.*, 22, 85–88, 1995.

[50] Morill, J. S., and W. M. Benesh, Auroral N2 emissions and the effect of collisional processes on N2 triplet state vibrational populations, *J. Geophys. Res.*, 101, 261–274, 1996.

[51] Nemzek,, R. J., and J. R. Winckler, Observation and integration of fast sub-visual light pulses from the night sky, *Geophys. Res. Lett.*, 16, 1015–1019, 1989.

[52] Nicolet, M., R. R. Meier, and D. E. Anderson, Radiation Field in the Troposphere and Stratosphere — II. Numerical Analysis, *Planet. Space. Sci.*, 30, 935–941, 1982.

[53] Niemeyer L., L. Pietronero, H. J. Wiesmann, Fractal Dimension of Dielectric Breakdown, *Phys. Rev. Lett.*, 52, 12, p. 1033, 1984.

[54] Ogawa, T., and M. Brook, The mechanism of the intracloud lightning discharge, *J. Geophys. Res.*, 69, 5141–5150, 1964.

[55] Ott, E, *Chaos in dynamical systems*, Cambridge University Press, 1993.

[56] Papadopoulos, K., G. Milikh, A. Gurevich, A. Drobot, and R. Shanny, Ionization rates for atmospheric and ionospheric breakdown, *J. Geophys. Res.*, 98(A10), 17,593–17,596, 1993a.

[57] Papadopoulos, K., G. Milikh, and P. Sprangle, Triggering HF breakdown of the atmosphere by barium release, *Geophys. Res. Lett.*,20, 471–474, 1993b.

[58] Papadopoulos, K., G. Milikh, A. W. Ali, and R. Shanny, Remote photometry of the atmosphere using microwave breakdown, *J. Geophys. Res.*, 99(D5), 10387–10394, 1994.

[59] Papadopoulos, K., G. M. Milikh, J. A. Valdivia, Comment on "Can gamma radiation be produced in the electrical environment above thunderstorms", *Geophys., Res. Lett.*, 23, 17, p. 2283, 1996.

[60] Pasko, V. P., U. S. Inan, Y. N. Taranenko, and T. Bell, Heating, ionization and upward discharges in the mesosphere due to intense quasi-electrostatic thundercloud fields, *Geophys. Res. Lett.*,22, 365–368, 1995.

[61] Rowland, H. L., R. F. Fernsler, and P. A. Bernhardt, Ionospheric breakdown due to lightning driven EMP, submitted to *J. Geophys. Res.*, 1994.

[62] Roussel-Dupre R. A. , A. V. Gurevich, T. Tunnel, and G. M. Milikh, Kinetic theory of runaway breakdown, *Phys Rev. E*, 49, 2257, 1994.

[63] Roussel-Dupre, R. A., A. V., Gurevich, On runaway breakdown and upward propagating discharges, *J. Geophys. Res.*, 101, 2297–2311, 1996.

[64] Royden, H. L., *Real Analysis*, Prentice Hall, 1963.

[65] Sander, L. M., *Fractal growth process*, Nature, 322, 1986.

[66] Sentman, D. D., and E. M. Wescott, Observations of upper atmospheric optical flashes recorded from an aircraft, *Geophys. Res. Lett.*, 20, 2857–2860, 1993.

[67] Sentman, D. D., The middle atmosphere: a porous buffer separating the lower and upper atmospheres (abstract), *EOS Trans. AGU*, 75, Spring Meeting Suppl., p. 49, 1994.

[68] Sentman, D. D., E. M. Wescott, D. L. Osborne, D. L. Hampton, and M. J. Heavner, Preliminary results from the sprites94 aircraft campaign, 1, red sprites, *Geophys. Res. Lett.*, 22, 1205–1208, 1995.

[69] Short, R., P. Lallement, D. Papadopoulos, T. Wallace, A. Ali, P. Koert, R. Shanny, and C. Stewart, Physics studies in artificial ionospheric mirror (AIM) related phenomena, *Tech. Rep.* GL–TR–90–0038, Geophysics Lab., Air Force Systems Command, Hansom Air Force Base, Mass, 1990.

[70] Taranenko, Y., R. Roussel-Dupre, High altitude discharges and gamma-ray flashes: a manifestation of runaway air breakdown, *Geophys., Res. Lett.*, 23, 5, p.571, 1996.

[71] Tsang, K., K. Papadopoulos, A. Drobot, P. Vitello, T. Wallace, and R. Shanny, RF ionization of the lower ionosphere, *Radio Science.*, 20(5), 1345–1360, 1991.

[72] Uman, M. A., *The Lightning Discharge*, Academic Press, Orlando 1987.

[73] Van Zyl, B., and W. Pendleton Jr., , and production in e— + N2 collisions, *J. Geophys. Res.*, 100, 23,755–23,762, 1995.

[74] Vaughan, Jr., O. H., R. Blakeslee, W. L. Boeck, B. Vonnegut, M. Brook, and J. McKune, Jr., A cloud-to-space lightning as recorded by the Space Shuttle payload-bay TV cameras, *Mon. Weather Rev.*, 120, 1459–1461, 1992.

[75] Vecchi, G., D. Labate, F. Canavero, Fractal approach to lightning radiation on a tortuous channel, *Radio Science*, 29, p. 691, 1994.

[76] Werner, D. H., and P. L. Werner, On the synthesis of fractal radiation patterns, *Radio Science,* 30, 29–45, 1995.

[77] Wescott, E. M., D. Sentman, D. Osborne, D. Hampton, M. Heavner, Preliminary Results from the Sprite94 aircraft campaign, 2, blue jets, *Geophys. Res. Lett.*, 22, 10, p.1213, 1995.

[78] Williams, E. R., The electrification of thunder storms, *Scientific American*, 88–99, November 1988.

[79] Wilson, C. T. R., The acceleration of -particles in strong electric fields such as those of thunderclouds, *Proc. Cambridge Phys. Soc.*, 22, 534–538, 1924.

[80] Winckler, J. R., R. C. Franz, and R. J. Nemzek, Fast low–level light pulses from the night sky observed with the SKYFLASH program, *J. Geophys. Res.*, 98(D5), 8775–8783, 1993.

[81] Winckler, J. R., Further observations of cloud-ionosphere electrical discharges above thunderstorms, *J. Geophys., Res.*, 100, 14335, 1995.

[82] Winckler, J. R., W. A. Lyons, T. E. Nelson, and R. J. Nemzek, New high-resolution ground-based studies of sprites, *J. Geophys. Res.*, 101, 6997, 1996.

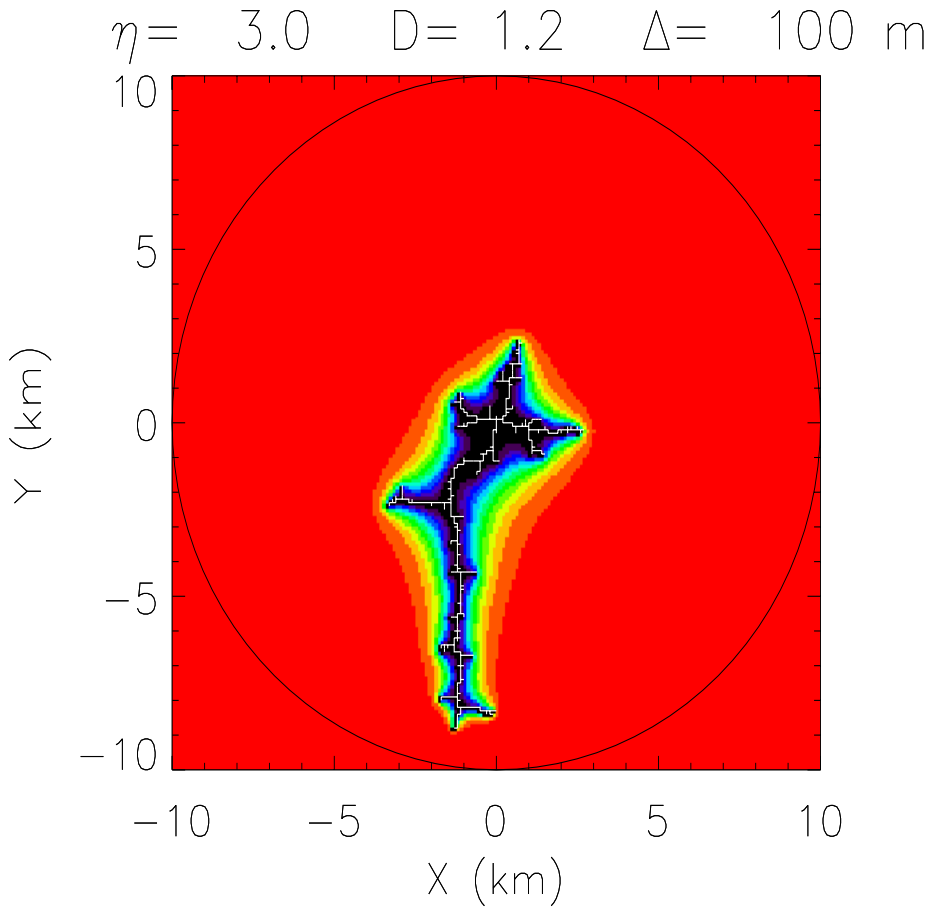

Figure 17: Fractal discharge generated for $\eta = 3$.

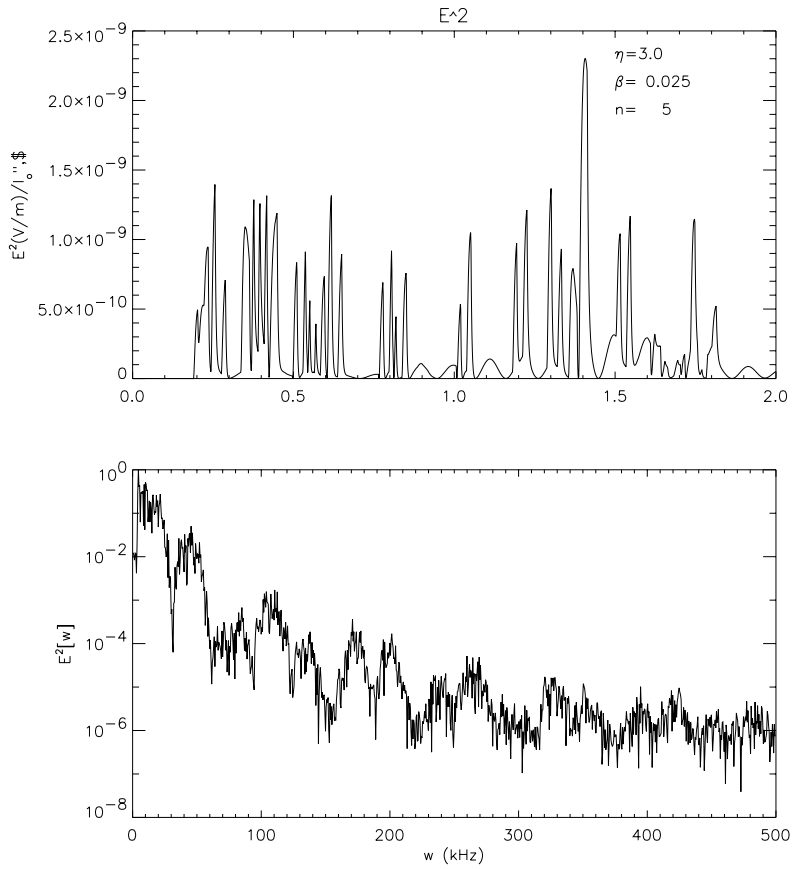

Figure 18: (a) The field power density due to the stochastic discharge model at a given position as a function time (b) and the frequency spectrum of the field.

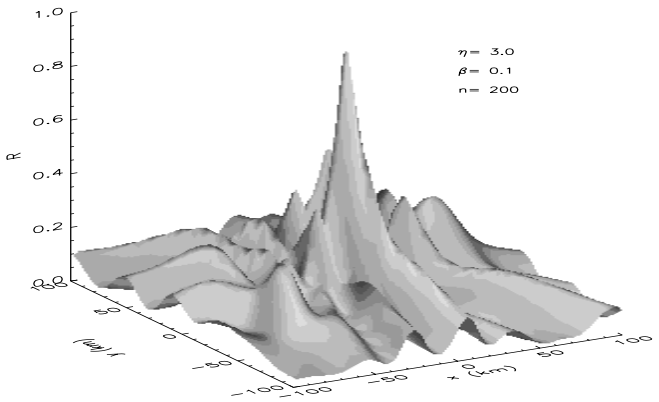

Figure 19: The array factor for $\eta = 3$.

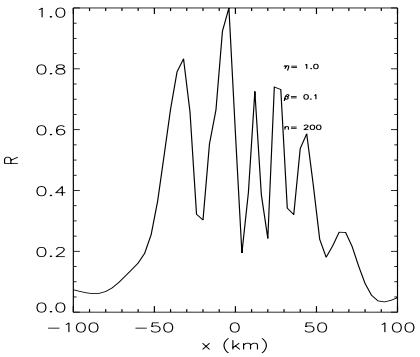

Figure 20: Cross-section of the array factor for $\eta = 1$.

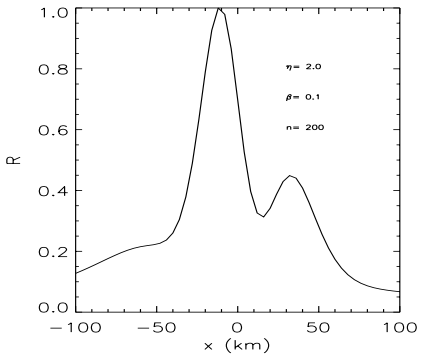

Figure 21: Cross-section of the array factor for $\eta = 2$.

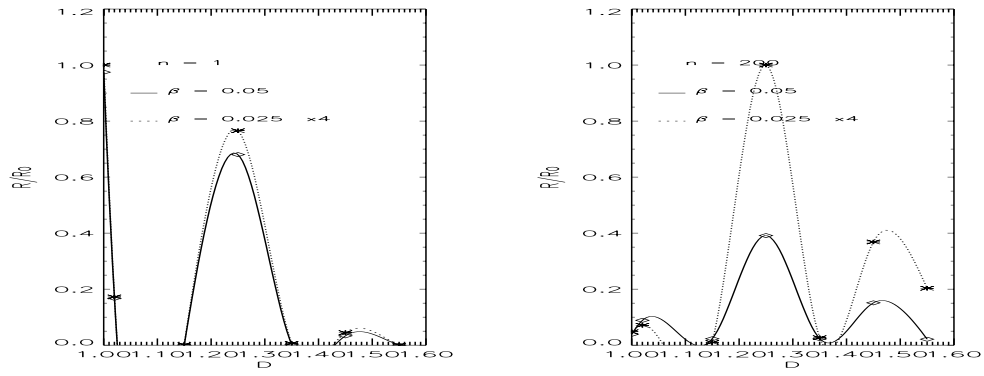

Figure 22: The array factor (a) For $n_f = 1$ and (b) for $n_f = 200$. The graph has been interpolated for the purpose of illustration.

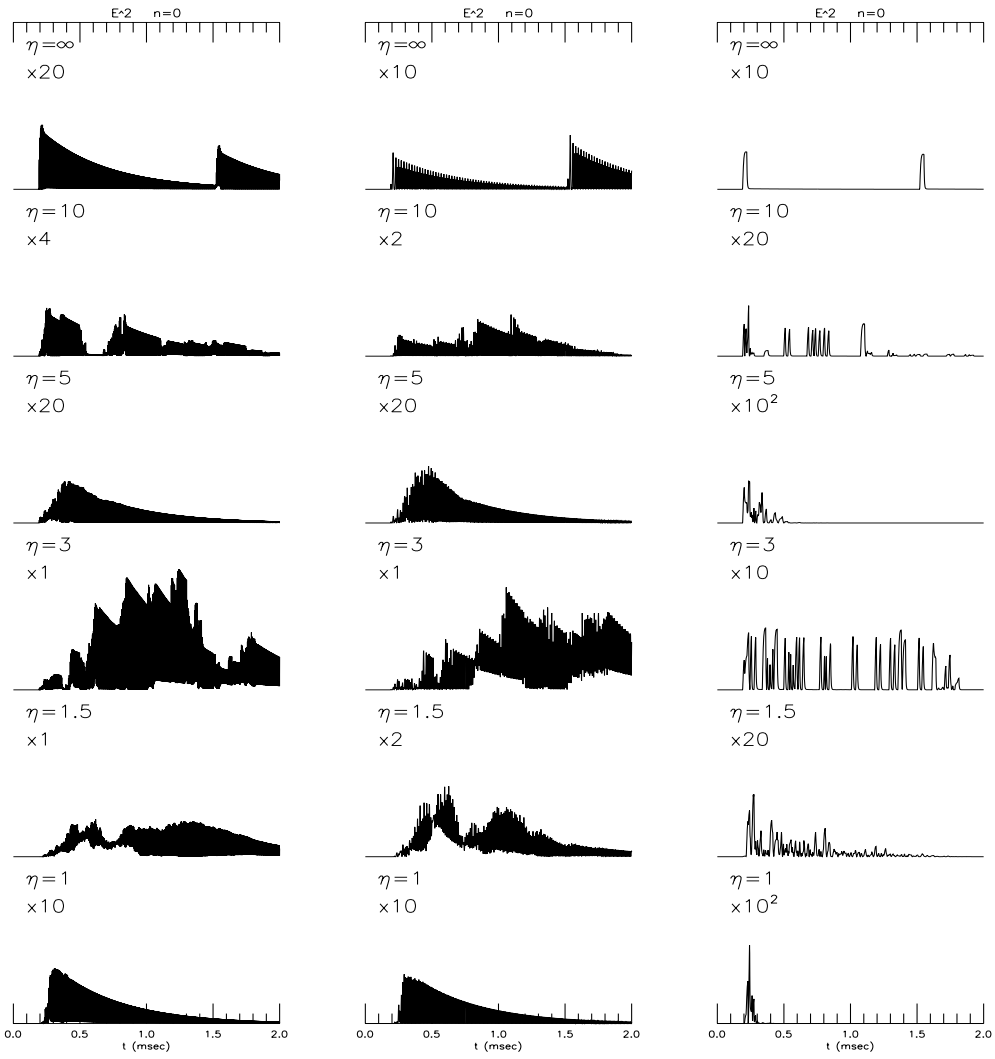

Figure 23: The time dependence of the radiation fields for the fractal models. See explanation in text.

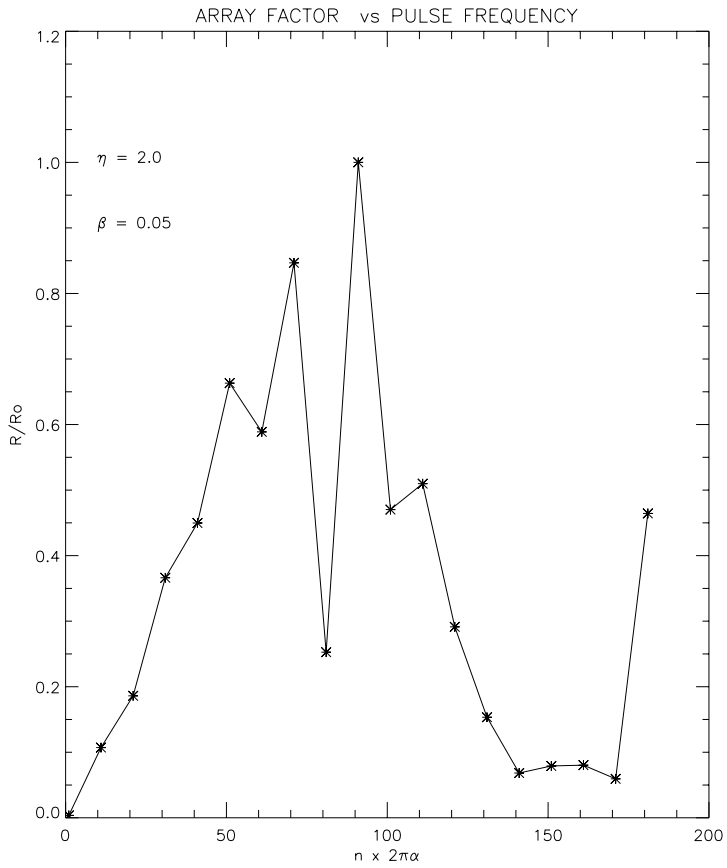

Figure 24: The array factor as a function of n_f for $\eta = 3$.

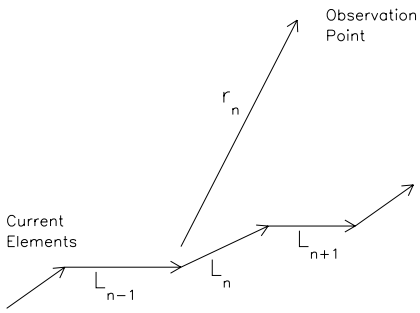

Figure 25: A diagram that explains all the variables and coefficients